ARTICLE

Structural and theoretical insights into solvent effects in an iron(III) SCO complex

Raúl Díaz-Torres,[a][†] Theerapoom Boonprab,[a] Silvia Gómez-Coca,[b] Eliseo Ruiz,[b] Guillaume Chastanet,[c] Phimphaka Harding*[a] and David J. Harding*[a]

Alcohol effects in a series of iron(III) spin crossover complexes [Fe(qsal-Cl)$_2$]NO$_3$·ROH (R = Me **1**, Et **2**, 1-Pr **3**) are explored. Despite the solvents differing from each other by only one or two CH$_2$ groups, unique packing motifs are observed for each complex. While **1** crystallizes in triclinic $P\overline{1}$ with two independent iron(III) centres, connecting them in a tight undulating 1D chain with a rectangular cross-section; **2** (monoclinic $P2_1/c$) and **3** (monoclinic $I2/a$) crystallize with only one iron center. For **2**, a linear 1D chain is observed with a square cross-section, while **3** exhibits a looser 1D chain formed by dimers. The 3D supramolecular networks are distinctive with **1** showing identical parallelogram shaped 2D sheets, whereas **2** and **3** show alternating 2D sheets with differing staggering between the layers (AB). These results are supported by Hirshfeld surface analysis. The magnetic studies show no significant SCO for **1** and **3**. However, **2** shows an incomplete gradual spin transition (T$_{1/2}$ = 200 K). Moreover, upon partial ethanol desolvation, a 25 K hysteresis near room temperature (T$_{1/2}\downarrow$ = 275 K, T$_{1/2}\uparrow$ = 300 K) is observed. The packing observed in **2** is present in many other [Fe(qsal-X)$_2$]$^+$ complexes with hysteresis and abrupt SCO. DFT calculations using the r^{2}SCAN functional quantify the differences for the **1** and **2** in the low-high spin energy and their cooperative effects. This study illustrates that even small changes in the solvent can dramatically influence the crystal packing and therefore the SCO properties.

Introduction

The interest in molecular devices is constantly growing as industry demands new devices to address our present and future technological needs.[1–4] Spin crossover (SCO) complexes exhibit bistability, and as molecular switches, they can be used as active components in memory devices or molecular sensors.[5] Switching occurs between two different electronic states: high spin (HS) and low spin (LS) under the application of certain external stimuli. Concomitant with the spin transition, there are changes in magnetism, size and colour. However, despite of the large number of reported SCO compounds, workable devices are still a challenge.[4] The main reason relates to the difficulty in designing suitable compounds due to the multitude of factors that influence the SCO properties.[6] Firstly, the ligand must

generate a suitable ligand field, and engage in strong intermolecular interactions, for instance hydrogen bonds,[7–9] π-π interactions,[10] and halogen bonds.[11–13] Collectively these interactions determine the cooperativity. Depending on the degree of cooperativity, different types of transition will be obtained: incomplete, gradual, or abrupt, possibly with hysteresis, the latter being the most interesting in terms of applications. In addition to the ligand, the SCO behaviour is strongly influenced by the anion and solvent.[14–20] Generally, changing the anion completely alters the packing and therefore, the SCO properties. In contrast, solvent effects tend to be more subtle, with minor modifications of the lattice. One of the first examples of the impact of solvent on SCO materials was reported in 2002 by Kepert *et al*. who showed that different alcohols could be absorbed into a 2D framework material switching on SCO.[21] Since then, many studies have shown a variety of solvent effects, even in molecular materials.[18,22] In some systems SCO becomes more abrupt upon solvent exchange,[22–25] while in others the SCO becomes stepped or even hysteretic.[26,27] Indeed, in [Fe(tolpzph)$_2$(NCS)$_2$]·THF (tolpzph = 4-p-tolyl-3-(phenyl)-5-(2-pyrazinyl)-1,2,4-triazole) it is even possible to quantitatively sense the solvent.[28] However, in most of these studies the solvents were of different sizes or geometry, and supramolecular connectivity, making it difficult to discern the relative influence of each factor.

In seeking to address this problem, the present work explores the influence of different alcohols on the SCO

a. *Functional Materials and Nanotechnology Centre of Excellence, Walailak University, Thasala, Nakhon Si Thammarat, 80160, Thailand. E-mail: hdavid@mail.wu.ac.th or kphimpha@mail.wu.ac.th*
b. *Departament de Química Inorgànica i Orgànica, Institut de Recerca de Química Teòrica i Computacional, Universitat de Barcelona, Diagonal 645, 08028 Barcelona, Spain*
c. *Institut de Chimie de la Matière Condensée de Bordeaux, Université de Bordeaux, 87 Av. Doc. A. Schweitzer, F-33608 Pessac, France*
† Now at Thammasat University Research Unit in Multifunctional Crystalline Materials and Applications (TU-MCMA), Faculty of Science and Technology, Thammasat University, Pathum Thani 12121, Thailand
Electronic Supplementary Information (ESI) available: [details of any supplementary information available should be included here]. See DOI: 10.1039/x0xx00000x

properties of an iron(III) SCO complex, [Fe(qsal-Cl)$_2$]NO$_3$·ROH (qsal-Cl = 4-chloro-2-[(8-quinolylimino)methyl]phenolate; ROH = Me **1**, Et **2**, 1-Pr **3**). The [Fe(qsal-X)$_2$]anion family was chosen as it is among the best explored in iron(III) SCO chemistry with studies covering anion, substituent and solvent effects providing an excellent library of comparative complexes.[17,19,29–31] We demonstrate that the different alcohols impact the packing and thus the SCO properties of the system providing insight that may lead to more designed systems in the future.

Experimental Section

Materials

All reactions were carried out in aerobic conditions using commercial grade solvents for the synthesis of all compounds. The Hqsal-Cl ligand was synthesized as described previously.[32] All other chemicals were purchased from TCI Chemicals or Sigma-Aldrich and used as received.

Synthesis of [Fe(qsal-Cl)$_2$]NO$_3$·MeOH 1

Hqsal-Cl (56.5 mg, 0.2 mmol) was dissolved in dichloromethane (3 mL) giving an orange solution. NEt$_3$ (28 μL, 0.2 mmol) was added and the solution was stirred for 5 min resulting in a change to dark orange. Next, blank MeOH (5 mL) was layered on the top of the Hqsal-Cl solution. In a separate flask, Fe(NO$_3$)$_3$·9H$_2$O (40.4 mg, 0.1 mmol) was dissolved in MeOH (5 mL), filtered and then layered on the top of the previous solution and left for 4 days. Black crystals were obtained which were washed with hexane and air-dried (51 mg, 75 %). Anal. Calcd. for C$_{32}$H$_{20}$Cl$_2$FeN$_5$O$_5$·CH$_4$O (713.27 g·mol^{-1}): C 55.56 %, H 3.39 %, N 9.82 %. Found: C 55.70 %, H 3.05 %, N 10.35 %. ESI$^+$ (m/z): 618.0 [Fe(qsal-Cl)$_2$]$^+$. IR Data (KBr, cm^{-1}): 3043 (ν_{C-H}), 1595 ($\nu_{C=N}$), 1384 (ν_{N-O}).

Synthesis of [Fe(qsal-Cl)$_2$]NO$_3$·EtOH 2

The same procedure as above was used substituting MeOH for EtOH (56 mg, 82 %). Anal. Calcd. for FeC$_{32}$H$_{20}$Cl$_2$N$_5$O$_5$·C$_2$H$_4$O (727.30 g·mol^{-1}): C 56.14 %, H 3.60 %, N 9.63 %. Found: C 56.24 %, H 3.29 %, N 10.09 %. ESI$^+$ (m/z): 618.0 [Fe(qsal-Cl)$_2$]$^+$ IR Data (KBr, cm^{-1}): 3033 (ν_{C-H}), 1598 ($\nu_{C=N}$), 1382 (ν_{N-O}).

A small number of crystals of **2·H$_2$O** were isolated after slow evapouration of the mother liquor. Heating of the crystals to 360 K readily yielded **2ns**. We were unable to prepare this compound in sufficient quantities for elemental analysis and hence we include only the crystal structure for comparative purposes.

Synthesis of [Fe(qsal-Cl)$_2$]NO$_3$·1-PrOH 3

The same procedure as in **1** substituting MeOH for 1-PrOH (55 mg, 80 %). Anal. Calcd. for FeC$_{32}$H$_{20}$Cl$_2$N$_5$O$_5$·C$_3$H$_8$O (741.38 g·mol^{-1}): 56.70 %, H 3.81 %, 9.45 %. Found: C 56.64 %, H 3.74 %, N 9.68 %. ESI$^+$ (m/z): 618.0 [Fe(qsal-Cl)$_2$]$^+$ IR Data (KBr, cm^{-1}): 3031 (ν_{C-H}), 1596 ($\nu_{C=N}$), 1383 (ν_{N-O}).

X-ray Crystallography

The diffraction data of **1**-**3** were collected on a Rigaku SuperNova diffractometer with a HyPix 3000 detector using CuKα radiation (λ = 1.54184 Å).[33] Data reduction, scaling, and absorption corrections were performed using CrysAlisPro.[34] The structures were solved, and the space groups $P\overline{1}$, $P2_1/c$, $P2_1/n$ and $I2/a$ were determined for **1**, **2**, **2ns** and **3**, respectively, by intrinsic phasing using ShelXT and refined by full matrix least-squares minimization on F^2 using SHELXL.[35,36] All non-hydrogen atoms were refined anisotropically. Hydrogen atoms were included in calculated positions and refined with isotropic thermal parameters, which were 1.2x or 1.5x the equivalent isotropic thermal parameters of their parent carbon or oxygen atoms. In the case of **2** at 280 K and **3** at all temperatures a solvent mask was applied to account for diffuse electron density. All pictures were generated with OLEX2.[37] Crystallographic data for the structures have been deposited with the Cambridge Crystallographic Data Centre (CCDC) 2175687-2175695. Powder X-ray diffraction data were measured on a Rigaku SuperNova diffractometer with a HyPix 3000 detector using CuKα radiation (λ = 1.54184 Å). The samples were gently ground and then suspended in Fomblim Y oil, and the data were collected between 2θ = 5–50°.

Physical measurements

Infrared spectra (4000–400 cm^{-1}) were recorded as KBr pellets on a Bruker Tensor 27 FT-IR spectrometer with OPUS data collection program. Elemental analyses were carried out using a Eurovector EA3000 analyzer. ESI-MS were carried out on a Bruker AmaZon X LCMS Mass Spectrometer. Magnetic measurements were carried out with a Quantum Design SQUID MPMS 7XL device operating from 10 K to 390 K at 20 kOe of applied magnetic field. The temperature scan rate was fixed at 0.4 K/min. Polycrystalline samples were introduced in a polypropylene bag that was mounted in a capillary tube made of polyimide. The diamagnetic contribution of the bag was corrected from blank measurements and the diamagnetic corrections for the measured compounds were estimated from Pascal Tables

DFT calculations

DFT calculations were performed with the all-electron FHI-aims computer code (*tight* option).[38] The geometry optimizations were carried out using the periodic structures only Gamma k-point using the PBE exchange-correlation functional[39] including dispersion contributions[40] (CIF files of the optimized structures may be found in the ESI). The state energies were calculated using the r^{2}SCAN functional[41] that have been proposed as the best option for the energetics of spin crossover systems.[42]

Results and discussion

Synthesis and IR spectroscopy

The complexes were synthesized by layering a solution of Fe(NO$_3$)$_3$·9H$_2$O in MeOH **1**, EtOH **2** or 1-PrOH **3** over a solution of Hqsal-Cl in dichloromethane, with base added. Crystals were obtained for all the complexes in good yield. Slow evaporation of **2** resulted in very small amounts of the H$_2$O solvate, which upon heating to 360 K, gave rise to the desolvated complex, [Fe(qsal-

Cl)$_2$]NO$_3$ **2ns**. The IR spectra show a strong stretch at *ca.* 1600 cm^{-1} assignable to the imine group of the qsal-Cl ligand.[32] The anion stretch is observed at 1382-1384 cm^{-1}, as expected for a free anion.[43] At higher energies, the stretches for the O-H group of the alcohol solvents are observed at *ca.* 3300 cm^{-1}.

Structural studies

X-ray crystallographic studies of [Fe(qsal-Cl)$_2$]NO$_3$·ROH (R = Me **1**, Et **2**, 1-Pr **3**) were conducted at 150 K and 280 K to study their SCO behaviour. In all cases, structural studies beyond 280 K to get the desolvated complex were unsuccessful due to a loss of crystallinity. PXRD studies show that the crystal structures of **1-3** are reflective of the bulk material (Figure S1).

Complex **1** crystallizes in triclinic *P*$\overline{1}$, while **2, 2ns** and **3** exhibit monoclinic symmetry (space groups *P2$_1$/c, P2$_1$/n and I2/a*, respectively). Interestingly, the asymmetric unit in **1** reveals two crystallographically independent Fe^{III} centers (Fe1 and Fe2) along with two counteranions and two methanol molecules. Meanwhile **2**, **2ns** and **3** have only one Fe^{III} center, one counteranion and one molecule of the corresponding solvent in the case of **2** and **3** (EtOH **2**, 1-PrOH **3**). In **1** at Fe2, one of the qsal-Cl ligands shows substantial disorder of the quinoline ring and in one of the nitrate anions. A more pronounced disorder of the anion and solvent is found in **2**, while for **3** a solvent mask was required as the 1-PrOH was severely disordered. In all cases, the Fe^{III} center is coordinated in an octahedral environment with two qsal-Cl ligands orthogonal to each other in a *mer* fashion. Selected Fe-N/O bonds, cell volumes and octahedral distortion parameters are given in Table S1 and Figure 1 shows the structures of **1** and **2** at 150 K.
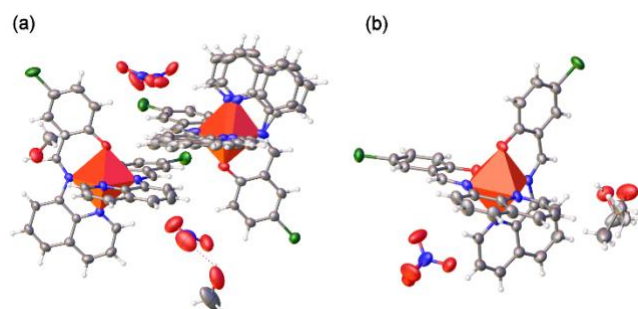

Fig 1. Asymmetric unit in **1** (left) and **2** (right) at 150 K. Ellipsoids are drawn at 50 %.
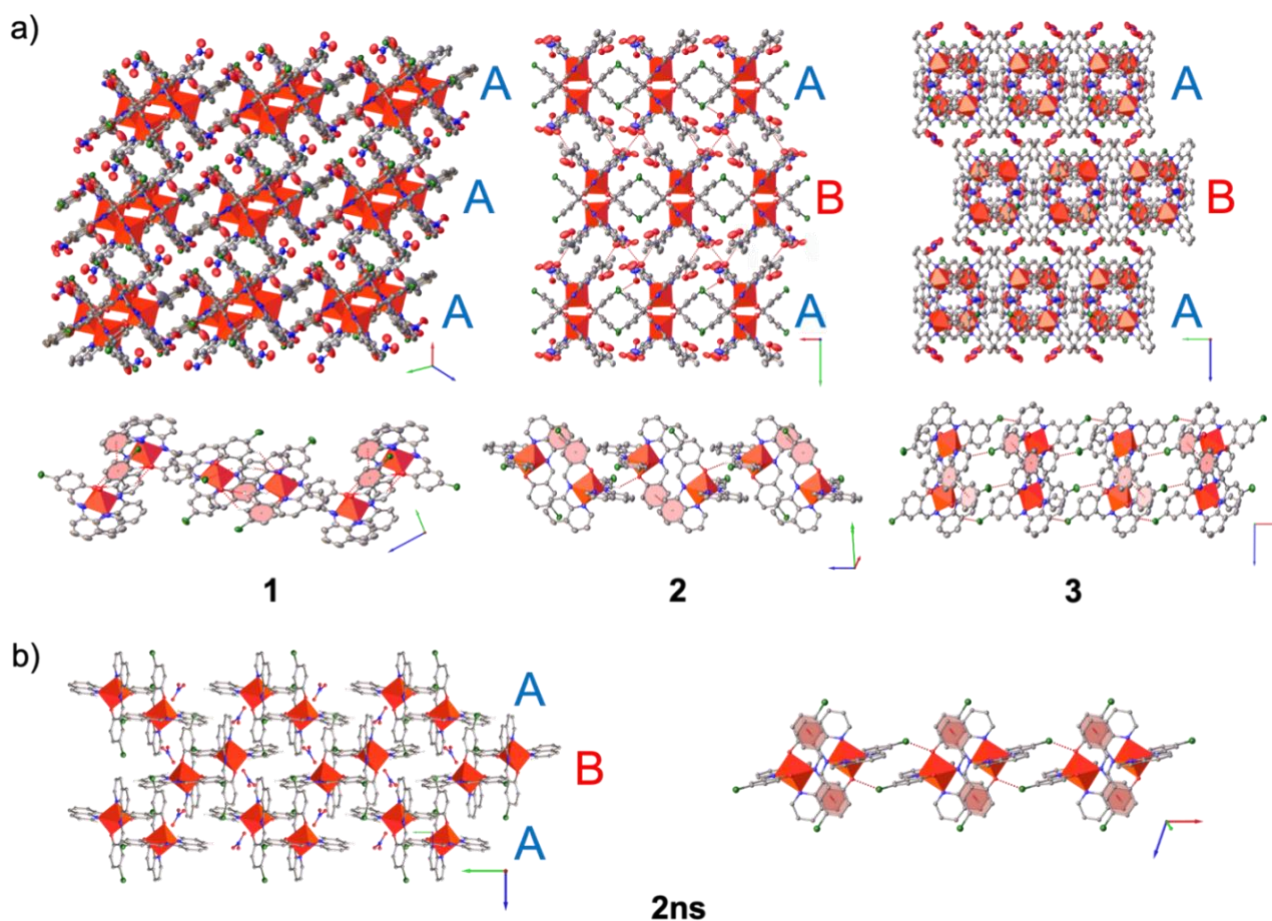

Fig 2. Structural representation of the supramolecular interactions of 1D chain (bottom) and 3D supramolecular network (top) for (a) **1** (left), **2** (middle) and **3** (right) at 150 K. (b) **2ns** 3D supramolecular network (left) and 1D chain (right) at 200 K. Disordered atoms and hydrogens that are not involved in the interactions are omitted.

At low temperature, the four systems show similar Fe-N/O distances *ca.* 1.95-1.97 Å and 1.87-1.88 Å, respectively, consistent with LS Fe^{III} giving a [LS-LS] state for **1**, and LS for **2**, **2ns** and **3**. Heating to 280 K causes no significant changes in the Fe-N/O distance for **3**, indicating no SCO behavior. For **1**, the Fe1 center shows no changes while a slight increase is found at Fe2 (ΔFe-N_{av} 0.092 Å and ΔFe-O_{av} 0.012 Å). This is consistent with the magnetic measurements, where only a slight increase in the magnetic susceptibility is observed (*vide infra*). However, in the case of **2** and **2ns**, a significant increase of the Fe-N/O distance is observed (ΔFe-N_{av} 0.145 Å and ΔFe-O_{av} 0.019 Å), indicating that the Fe^{III} center is mostly HS at 280 K and 360 K, respectively.[44] The octahedral distortion parameters (Σ and Θ) are in agreement with the above spin state assignments, particularly Θ, where a more significant change is observed for **2** (Θ_{150K} = 135; Θ_{280K} = 225) and **2ns** (Θ_{200K} = 123; Θ_{360K} = 193).[45]

Structural packing

As found in many [Fe(qsal-X)$_2$]$^+$ systems, the metal centers are connected into a 1D chain via orthogonal π-π interactions, confirming the robustness of this motif.[12,16,23,46] However, certain differences are observed that depend on the solvent of crystallization.

In the case of **1**, the metal centers pack forming an undulating 1D chain via three different π-π interactions involving Fe1-Fe1 centers (Type A), Fe2-Fe2 centers (Type B) and Fe1-Fe2 centers (Type C), two C-H$\cdots$O interactions and one additional C-H$\cdots$Cl interaction (Figure 2, left). This arrangement has also been observed in [Fe(qsal-F)$_2$]anion (anion = NCS, BF$_4$, ClO$_4$, PF$_6$, NO$_3$, OTf).[16] The cross-section is rectangular (Figure 2), resulting in different Fe-Fe distances (ΔFe-Fe = 0.92 Å). For **2**, the 1D chain is supported by one type of π-π interaction and two C-H$\cdots$O interactions, with a square cross-section (Figure 2, middle) and similar Fe-Fe distances within the chain (ΔFe-Fe = 0.17 Å). The same 1D chain is found in [Fe(qsal-Cl)$_2$]NCS·MeOH.[46] However, the Fe-Fe distances are shorter than those in **2** (ΔFe-Fe = 0.11 Å), perhaps explaining the more gradual SCO in **2**, compared with the stepped SCO for the NCS system. In **2ns**, the 1D chain is supported by a pair of Cl$\cdots$O halogen bonds resulting in a wide rectangular cross-section with different Fe-Fe distances within the chain (Figure 2, bottom; ΔFe-Fe = 3.60 Å). For **3**, dimers are formed supported only by π-π interactions, which are further connected by weak C-H$\cdots$Cl interactions, creating clear gaps in the linear 1D chain (Figure 2, right). These gaps are mainly occupied by disordered 1-PrOH molecules. It is important to note that, as the temperature increases, the π-π interactions become longer if the metal center undergoes SCO (Table S3). In **2** and **2ns**, the π-π (Type A) distance increases from 3.36 to 3.39 Å and 3.46 to 3.50 Å, respectively, while for **1** (Fe2 center), the π-π (Type B) increases from 3.22 to 3.36 Å. Conversely, in the case of **3** and **1** (Fe1 center), there is a decrease in these values consistent with the lack of SCO behavior at these centers.[46]

Beyond the packing of the 1D chain, C-H$\cdots$Cl interactions are essential in connecting the chains to form the 3D supramolecular network (Figure 2 and S2-S3). Moreover, a Cl$\cdots$O halogen bond involving the nitrate anion is observed in **1**. Halogen bonding also appears in [Fe(qsal-Br)$_2$]NO$_3$·MeOH,[47] helping to improve

cooperativity (stepped SCO), while in **1** the effect is minimal, reflecting the smaller σ hole typically found for Cl.[48] Notably, the neighboring chains for **2ns** are connected by C-H$\cdots$O interactions involving the nitrate anion (Figure S3).

As can be seen in Figure 2 (top), a remarkable difference is observed in the construction of the 3D network. For **1**, identical parallelogram shaped 2D sheets are observed. In the case of **2, 2ns** and **3**, the 2D sheets are stacked alternately. However, the degree of distortion between the 2D planes (AB) is significantly different in each case. Interestingly, the particular packing observed in **2** with the very regular arrangement is present in many other [Fe(qsal-X)$_2$]$^+$ complexes that exhibit abrupt and hysteretic SCO and seems to be a common feature in these systems *(vide infra)*.[16,46,47] In **2ns**, the packing is unique and has not previously been observed in any [Fe(qsal-X)]$^+$ system. The planes are interdigitated (Figure S4), with plane A linked to the lower plane A by C-H$\cdots$Cl interactions and to the plane B by C-H$\cdots$O interactions, involving the nitrate anion (Figure S5). Moreover, multiple π-π interactions as well as C-H$\cdots\pi$ interactions are also observed, resulting in a rather tightly packed structure (Figure S6).

The difference in their arrangements has a direct influence on the compactness of the network, easily evidenced by the distance between the planes (d_{plane}) (Table S4). **1** shows the tightest structure (d_{plane} = 10.28 Å), followed by **2** (d_{plane} = 13.65 Å), **2ns** (d_{plane} = 14.35 Å and **3** (d_{plane} = 18.61 Å). In the case of **1**, the short distance might explain the stabilization of the LS state, as is also observed in [Fe(qsal-F)$_2$]NO$_3$. In contrast, the distance in **3** is significantly higher, and therefore the lack of SCO probably relates to the loss of connectivity. As expected, the trend in the d_{plane} values for **1-3** seems to be connected with the solvent size, as in all cases the solvent and the anion molecules are located between the planes, connecting the 2D planes by C-H$\cdots$O interactions (Figure S3). Unsurprisingly, as the network becomes looser, the solvent is found to be more disordered, requiring the use of solvent mask for **3**.

Overall, for each alcohol we observe unique packing, despite the solvents differing from each other by only one or two CH$_2$ groups. This is enough to completely modify the supramolecular packing and therefore their magnetic behavior *(vide infra)*. This contrasts with many other systems, where typically such small changes in the solvent results in isostructural systems.[49,50] A clear example can be seen in the [Fe(qsal-I)]OTf·solvent (solvent = MeOH, EtOH, n-PrOH, i-PrOH, acetone and MeCN), where despite the different solvents of crystallization, an almost identical packing is observed.[22]

Hirshfeld Analysis

For **1**, **2** and **2ns**, a Hirshfeld surface analysis was performed to provide deeper insight into the relationship between the intermolecular interactions and the SCO behavior.[51] For **3**, the analysis was not undertaken due to the application of the solvent mask. The Hirshfeld surface of **2** is shown in Figure 3, where the red spots represent the strongest intermolecular interactions. As can be seen, these red spots correspond mainly to O$\cdots$H interactions, however H$\cdots$H, C$\cdots$C and H$\cdots$Cl interactions are also present. The contribution of each one, as well as their strength are determined by the 2D fingerprint plots (Figure 3 and Table S5). The contributions

show that the changes in the interactions between **1** and **2** are minimal. For **2ns**, the O···H interaction is slightly weaker as it doesn't contain the H-bonds contribution from any solvent (Figure S7). The lack of difference between the interactions of **1** and **2** supports the above analysis, where the supramolecular packing is key to magnetic behaviour rather than individual interactions.
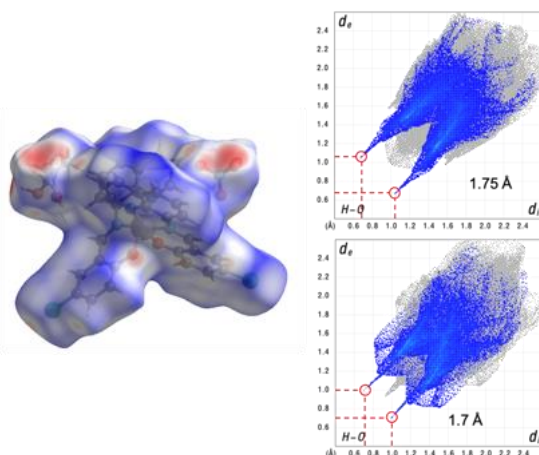

Fig 3. Hirshfeld surface mapped with d_{norm} of **2** (left), and 2D fingerprint of **2** (top) and **1** (bottom) of all contacts and O···H interactions.

Thermal stability and powder X-ray diffraction studies

TGA studies of **1**-**3** were undertaken with the results shown in Figure S8. The MeOH solvate shows a mass loss of 4.3 % (calculated 4.5 %) between the 300 and 340 K, consistent with one MeOH molecule. In **2**, a mass loss of 3% centered at 340 K occurs, indicative of loss of half an EtOH molecule (calculated 3.1 %). Continued heating results in a more gradual mass loss of 2.3 %, suggesting almost complete loss of the other half of the EtOH molecule, before the compound decomposes completely. In contrast, **3** shows complete solvent loss in a single step, but this time centered at 470 K.

To explore these changes further we undertook PXRD studies after heating the samples (350 K for **1**-**3** and 480 K for **3**) in the oven for 30 min (Figure S9-S11). The results are consistent with the TGA studies. For **1**, the diffraction pattern is different from **1**, and closely matches the simulated pattern of **2ns**, confirming the loss of solvent. In contrast for **2**, the PXRD shows slight changes from the simulated pattern of **2**, but no close match to **2ns** confirming that under these conditions only partial desolvation takes place, result in a new phase **2ps**. For **3**, the diffraction pattern matches **3**, indicating that it remains totally solvated after heating at 350 K. However, heating to 480 K results in a new diffraction pattern that is different from both **3** and **2ns**. This suggests that heating to this temperature results either in incomplete desolvation or the onset of decomposition.

Magnetic measurements

Variable temperature magnetic susceptibility studies were conducted on polycrystalline samples of **1**-**3** between 10-380 K for **2** (Figure 4) and 10-350 K for **1** and **3** (Figure 5), under a constant magnetic field of 20 kOe. At 10 K, the $\chi_M T$ values for **2**-**3** are *ca.* 0.5

cm^3 K mol^{-1} and slightly lower for **1** ($\chi_M T$ = 0.25 cm^3 K mol^{-1}). Despite the range of values, in all cases they are consistent with a LS Fe^{III} center. Heating up to 350 K, **1** and **3** show very gradual transitions (20 % HS and 30 % HS for **1** and **3**, respectively), consistent with the lack of SCO behavior observed crystallographically. In the case of **2**, the first heating until 350 K shows a reversible gradual transition (T$_{1/2}$ = 200 K), reaching a maximum value of 3.0 cm^3 K mol^{-1} (*ca.* 70% HS). This value is lower than would be expected for a full HS state Fe^{III} center, but is still consistent with the crystallographic data. However, when the sample is heated to 380 K, cooling now reveals an abrupt transition at T$_{1/2}\downarrow$ = 275 K. Heating from 200 to 320 K shows another abrupt transition this time at T$_{1/2}\uparrow$ = 300 K, with subsequent cooling confirming a hysteresis of 25 K. The change in the SCO behavior is most likely due to partial desolvation, in agreement with TGA analysis (Figure S8).
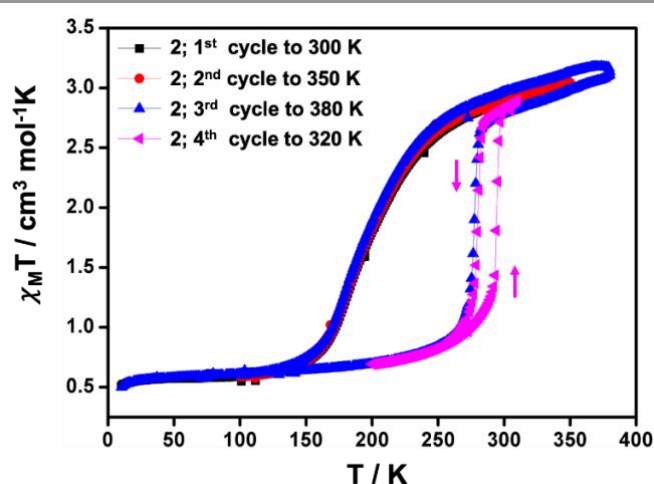

Fig 4. Thermal variation of $\chi_M T$ versus T plots for **2**: 1st cycle from 10 to 300 K (black), 2nd cycle from 10 to 350 K (red), 3rd cycle from 10 to 380 K (blue) and 4th cycle from 200 to 320 K (pink).

To explore the impact of heating on the samples additional measurements were undertaken. While no changes after several cycles are observed for **3** (Figure S12), indicating the robustness of the solvent in the crystal lattice as observed in the TGA; a small hysteresis loop of 10 K (T$_{1/2}\downarrow$ = 285 K, T$_{1/2}\uparrow$ = 295 K) is observed for **1** after heating up to 400 K (Figure S13). TGA (Figure S8) and PXRD studies (Figure S9), suggest that this change in the magnetic behavior is probably due to substantial desolvation of **1**. That the desolvation is not quite complete, is suggested by the fact that the maximum $\chi_M T$ value is 2.1 cm^3 K mol^{-1} at 400 K, and far lower than that expected based on the crystallographic data for **2ns**, where at 360 K the compound is mostly HS (Table S1). In the case of **2**, a similar magnetic profile is observed whether applying a vacuum or heating to higher temperature. This probably indicates a higher degree of desolvation, compared to heating to only 380 K (Figure S14-S15). As observed in the TGA and PXRD studies, only half of the ethanol molecules are lost easily. Hence, while in **3** the solvent seems to be tightly packed and no desolvation is observed, for **1** almost complete desolvation

occurs, with the ethanol solvate sitting in between these extremes. The different degrees of desolvation upon the various treatments of **2** directly impact the hysteresis and led us to undertake theoretical calculations to rationalize this behavior (*vide infra*).
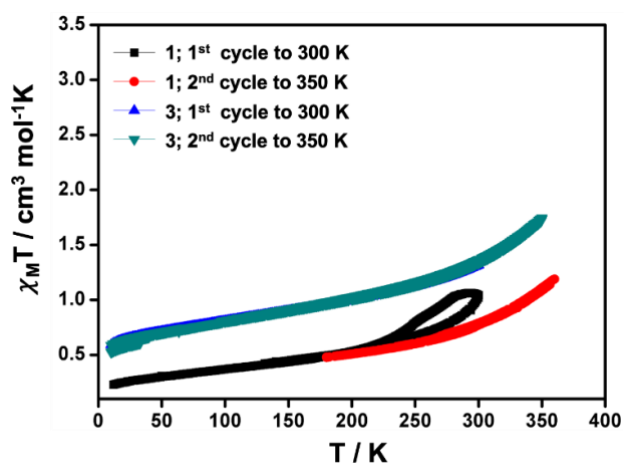

Fig 5. Thermal variation of $\chi_M T$ versus T plots for **1** and **3**: 1st cycle from 10 to 300 K (black for **1**, blue for **3**), 2nd cycle from 170 to 350 K (red for **1**) and from 10 to 350 K (green for **3**).

It is important to note that hysteresis is uncommon in SCO systems and those close to room temperature are even rarer.[52–56] Therefore, the hysteresis observed for the partially desolvated complex **2**, and the different magnetic behaviour of the three solvated complexes, make this complex a promising candidate for use in SCO devices to sense for the presence of alcohol molecules.

DFT calculations

To better understand the differences between the methanol and ethanol solvates and **2ns**, we undertook DFT calculations using the r^{2}SCAN exchange-correlation functional.[41] The optimized DFT unit cells of **1**, **2** and **2ns** in both spin states (see details experimental section and coordinates in ESI) show a good agreement with the experimental ones (see Table S6). For compound **2**, we also considered a system where two of the four ethanol molecules in the unit cell were removed (**2ps**). The reason for removing two ethanol molecules was based on the mass loss observed in the TGA discussed earlier (Figure S8). The calculated values related to the energetics of the SCO properties are shown in Table 1. The results show a higher low- and high-spin state difference for **1** consistent with the fact that SCO is only found in **2** and **2ps**. The energy for compound **2** is in the range of energies in which the entropic term becomes dominant as the temperature is increased.[57] The structural differences between the optimized **2** and **2ps** complex structures are very small but the E_{HS} - E_{LS} gap is slightly larger for **2ps** in agreement with the higher transition temperature for the system after the partial loss of solvent.

The coordination environment of the optimized HS and LS DFT structures for compounds **1** and **2** have been analysed by continuous shape measures.[58,59] The shape measurements relative to the octahedron geometry, S(O_h), for compound **1** are 0.237 and 0.270 for Fe1 and Fe2 respectively in the LS state, and 1.614 in both cases for the HS. Compound **2** shows S(O_h) values of 0.371 and 1.917 for LS and HS respectively. The increase from LS to HS is in agreement with previously found correlations between octahedricity and the magnetic moment of SCO compounds.[60] In the case of compounds with two meridionally coordinated tridentate ligands, the longer Fe-N distances in the HS state results in a decrease of the bite angles and a larger deviation from ideal octahedron. Additionally, values found for LS states are smaller for **1**, meaning that the geometries are closer to the ideal ones which is expected to be related to the larger energy of the antibonding e_g orbitals and agrees with **1** not showing SCO.

Table 1 Calculated low-high spin state energy differences (in kcal/mol per iron center) for **1**-**2** using the r^{2}SCAN exchange-correlation functionals. Positive values indicate a low-spin ground state. Calculated energy differences (in kcal/mol) with the r^{2}SCAN functional with four Fe^{III} centers, E$_1$ (energy difference 4HS-1LS3HS), E$_2$ (energy difference 1HS3LS-4LS) and H$_{coop}$ (E$_2$ -E$_1$).

	E_{HS} - E_{LS}	E$_1$	E$_2$	H$_{coop}$
1 (1 MeOH)	11.2	11.4	13.6	2.2
2 (1 EtOH)	8.3	7.6	9.6	2.0
2ps (0.5 EtOH)	8.6	5.9	11.0	5.1
2ns	10.1	9.1	10.9	1.8

To quantitatively analyze cooperative effects, we consider that the unit cells have four metal centers. This allows us to determine the H$_{coop}$ parameter proposed by Wolny and coworkers[61] as a quantitative measure of the cooperativity effects due to the environment in solid-state periodic systems. Such parameters can be quantified as the low-high spin state energy differences of a metal centre surrounded by high- (E$_1$) or low-spin (E$_2$) cations (see Table 1). Thus, E$_1$ is calculated as the energy difference of four high-spin Fe^{III} centres and the equivalent system with one centre in low-spin state (E$_2$ as the difference of all-metal centres in low-spin state and the case with one high-spin cation) (Figure S16-S19). The larger H$_{coop}$ for compound **2ps** (see Table 1) agrees with the hysteresis found experimentally when **2** loses two molecules of ethanol (see Figure 4 and S13). The increment in the cooperativity is generated when the partial loss of solvent is significant, since in the case of **1** similar values as **2** were obtained. From a structural point of view, the calculated intermolecular Fe⋯Fe distances in **2ps** from the optimized structures are around 0.05-0.1 Å shorter than in **2** and may also contribute to the higher cooperativity observed in this system. As noted above, **2ns** has larger Fe⋯Fe distances than **2**, which likely account for the weaker cooperativity. This supports the fact that the degree of solvation has an important impact on spin crossover behaviour.

Conclusions

In the present work we have studied the influence of alcohols on the SCO behavior of three iron(III) qsal-Cl complexes, [Fe(qsal-

$Cl)_2]NO_3 \cdot ROH$ (R = Me **1**, Et **2**, 1-Pr **3**). Surprisingly, despite the small differences between the solvents, a radically different packing is observed. While **1** shows a 1D chain with a rectangular cross-section and a tight supramolecular structure; **3** exhibits a looser structure where the metal centers are weakly connected by π-π interactions into dimers. In both cases, no significant SCO is observed. However, **2** seems to show an ideal balance in terms of compactness. The magnetic behavior shows an incomplete gradual spin transition at $T_{1/2}$ = 200 K. In addition, a drastic change in the magnetic properties is observed upon partial loss of ethanol, showing an abrupt transition near to room temperature with a 25 K hysteresis. Periodic DFT calculations show that the higher distortion of the coordination sphere from O_h symmetry of the Fe^{III} cations in **2** facilitates the spin transition. Furthermore, the calculations show larger cooperative effects when **2** partially loses solvent molecules. Therefore, this work shows that even small changes in the solvent may have a direct impact on the supramolecular packing, and consequently on their magnetic response. We believe that the findings from this work help to define more complete magnetostructural correlations in Fe-qsal-X SCO family which are likely to be useful in the design of devices and sensors based on these materials.

Author Contributions

Raúl Díaz-Torres: Investigation, Formal analysis, Data Curation, Visualization, Writing – Original Draft. **Theerapoom Boonprab**: Investigation, Data Curation. **Silvia Gómez-Coca**: Investigation, Formal analysis, Data Curation. **Eliseo Ruiz**: Methodology, Investigation, Formal analysis, Data Curation, Resources, Writing - Review & Editing, Funding acquisition. **Guillaume Chastanet**: Investigation, Formal analysis, Data Curation, Writing - Review & Editing. **Phimphaka Harding**: Conceptualization, Resources, Writing - Review & Editing, Supervision. **David J. Harding**: Conceptualization, Resources, Writing - Review & Editing, Supervision, Funding acquisition.

Conflicts of interest

There are no conflicts to declare.

Acknowledgements

Notes and references

1   H. Song, M. A. Reed and T. Lee, Single molecule electronic devices, *Adv. Mater.*, 2011, **23**, 1583–1608.

2   M. Ratner, A brief history of molecular electronics, *Nat. Nanotechnol.*, 2013, **8**, 378–381.

3   L. Sun, Y. A. Diaz-Fernandez, T. A. Gschneidtner, F. Westerlund, S. Lara-Avila and K. Moth-Poulsen, Single-molecule electronics: from chemical design to functional devices, *Chem. Soc. Rev.*, 2014, **43**, 7378–7411.

4   Y. Cao, S. Dong, S. Liu, Z. Liu and X. Guo, Toward functional molecular devices based on graphene-molecule junctions, *Angew. Chem. Int. Ed.*, 2013, **52**, 3906–3910.

5   A. Bousseksou, G. Molnár, L. Salmon and W. Nicolazzi, Molecular spin crossover phenomenon: recent achievements and prospects., *Chem. Soc. Rev.*, 2011, **40**, 3313–3335.

6   J.-F. Létard, P. Guionneau and L. Goux-Capes, in *Spin Crossover in Transition Metal Compounds III*, Springer-Verlag, Berlin/Heidelberg, pp. 221–249.

7   B. Weber, W. Bauer, T. Pfaffeneder, M. M. Dîrtu, A. D. Naik, A. Rotaru and Y. Garcia, Influence of hydrogen bonding on the hysteresis width in iron(II) spin-crossover complexes, *Eur. J. Inorg. Chem.*, 2011, 3193–3206.

8   I. Nemec, R. Herchel and Z. Trávníček, The relationship between the strength of hydrogen bonding and spin crossover behaviour in a series of iron(III) Schiff base complexes, *Dalton Trans.*, 2015, **44**, 4474–4484.

9   Z.-Y. Li, H. Ohtsu, T. Kojima, J.-W. Dai, T. Yoshida, B. K. Breedlove, W.-X. Zhang, H. Iguchi, O. Sato, M. Kawano and M. Yamashita, Direct Observation of Ordered High-Spin-Low-Spin Intermediate States of an Iron(III) Three-Step Spin-Crossover Complex, *Angew. Chem. Int. Ed.*, 2016, **55**, 5184–5189.

10   N. Nassirinia, S. Amani, S. J. Teat, O. Roubeau and P. Gamez, Enhancement of spin-crossover cooperativity mediated by lone pair–π interactions and halogen bonding, *Chem. Commun.*, 2014, **50**, 1003–1005.

11   K. Fukuroi, K. Takahashi, T. Mochida, T. Sakurai, H. Ohta, T. Yamamoto, Y. Einaga and H. Mori, Synergistic spin transition between spin crossover and spin-peierls-like singlet formation in the halogen-bonded molecular hybrid system: $[Fe(Iqsal)_2][Ni(dmit)_2] \cdot CH_3CN \cdot H_2O$, *Angew. Chem. Int. Ed.*, 2014, **53**, 1983–1986.

12   W. Phonsri, D. S. Macedo, C. G. Davies, G. N. L. Jameson, B. Moubaraki and K. S. Murray, Heteroleptic iron(III) Schiff base spin crossover complexes: halogen substitution, solvent loss and crystallite size effects, *Dalton Trans.*, 2017, **46**, 7020–7029.

13   S. E. Lazaro, A. Alkaş, S. J. Lee, S. G. Telfer, K. S. Murray, W. Phonsri, P. Harding and D. J. Harding, Abrupt spin crossover in iron(III) complexes with aromatic anions, *Dalton Trans.*, 2019, **48**, 15515–15520.

14   A. Tsukiashi, M. Nakaya, F. Kobayashi, R. Ohtani, M. Nakamura, J. M. Harrowfield, Y. Kim and S. Hayami, Intermolecular Interaction Tuning of Spin-Crossover Iron(III) Complexes with Aromatic Counteranions, *Inorg. Chem.*, 2018, **57**, 2834–2842.

15   B. A. Leita, S. M. Neville, G. J. Halder, B. Moubaraki, C. J.

Kepert, J. F. Létard and K. S. Murray, Anion-solvent dependence of bistability in a family of meridional N-donor-ligand-containing iron(II) spin crossover complexes, *Inorg. Chem.*, 2007, **46**, 8784–8795.

16   R. Díaz-Torres, W. Phonsri, K. S. Murray, L. Liu, M. Ahmed, S. M. Neville, P. Harding and D. J. Harding, Spin Crossover in Iron(III) Quinolylsalicylaldiminates: The Curious Case of [Fe(qsal-F)₂](Anion), *Inorg. Chem.*, 2020, **59**, 13784–13791.

17   K. Takahashi, K. Yamamoto, T. Yamamoto, Y. Einaga, Y. Shiota, K. Yoshizawa and H. Mori, High-Temperature Cooperative Spin Crossover Transitions and Single-Crystal Reflection Spectra of [Fe^III^(qsal)₂](CH₃OSO₃) and Related Compounds, *Crystals*, 2019, **9**, 81.

18   R. J. Archer, H. S. Scott, M. I. J. Polson, C. Mathonière, M. Rouzières, R. Clérac and P. E. Kruger, Solvent Dependent Spin-Crossover and Photomagnetic Properties in an Imidazolylimine Fe^II^ Complex, *Chem. - An Asian J.*, 2019, **14**, 2225–2229.

19   B. J. C. Vieira, L. C. J. Pereira, V. da Gama, I. C. Santos, A. C. Cerdeira and J. C. Waerenborgh, Correlation between Supramolecular Connectivity and Magnetic Behaviour of [Fe^III^(5-X-qsal)₂]⁺-Based Salts Prone to Exhibit SCO Transition, *Magnetochemistry*, 2021, **8**, 1.

20   A. Galet, A. B. Gaspar, M. C. Muñoz and J. A. Real, Influence of the counterion and the solvent molecules in the spin crossover system [Co(4-terpyridone)₂]Xₚ·nH₂O, *Inorg. Chem.*, 2006, **45**, 4413–4422.

21   G. J. Halder, C. J. Kepert, B. Moubaraki, K. S. Murray and J. D. Cashion, Guest-dependent spin crossover in a nanoporous molecular framework material, *Science*, 2002, **298**, 1762–1765.

22   W. Phonsri, P. Harding, L. Liu, S. G. Telfer, K. S. Murray, B. Moubaraki, T. M. Ross, G. N. L. Jameson and D. J. Harding, Solvent modified spin crossover in an iron(III) complex: Phase changes and an exceptionally wide hysteresis, *Chem. Sci.*, 2017, **8**, 3949–3959.

23   D. J. Harding, W. Phonsri, P. Harding, I. A. Gass, K. S. Murray, B. Moubaraki, J. D. Cashion, L. Liud and S. G. Telfer, Abrupt spin crossover in an iron(III) quinolylsalicylaldimine complex: Structural insights and solvent effects, *Chem. Commun.*, 2013, **49**, 6340–6342.

24   S. Rodríguez-Jiménez, H. L. C. Feltham and S. Brooker, Non-Porous Iron(II)-Based Sensor: Crystallographic Insights into a Cycle of Colorful Guest-Induced Topotactic Transformations, *Angew. Chem. Int. Ed.*, 2016, **55**, 15067–15071.

25   C. F. Herold, S. I. Shylin and E. Rentschler, Solvent-dependent SCO Behavior of Dinuclear Iron(II) Complexes with a 1,3,4-Thiadiazole Bridging Ligand, *Inorg. Chem.*, 2016, **55**, 6414–6419.

26   J. E. Clements, P. R. Airey, F. Ragon, V. Shang, C. J. Kepert and S. M. Neville, Guest-Adaptable Spin Crossover Properties in a Dinuclear Species Underpinned by Supramolecular Interactions, *Inorg. Chem.*, 2018, **57**, 14930–14938.

27   M. Fumanal, F. Jiménez-Grávalos, J. Ribas-Arino and S. Vela, Lattice-Solvent Effects in the Spin-Crossover of an Fe(II)-Based Material. the Key Role of Intermolecular Interactions between Solvent Molecules, *Inorg. Chem.*, 2017, **56**, 4474–4483.

28   R. G. Miller and S. Brooker, Reversible quantitative guest sensing via spin crossover of an iron(II) triazole, *Chem. Sci.*, 2016, **7**, 2501–2505.

29   B. J. C. Vieira, J. C. Dias, I. C. Santos, L. C. J. Pereira, V. Da Gama and J. C. Waerenborgh, Thermal hysteresis in a spin-crossover Fe^III^ quinolylsalicylaldimine complex, Fe^III^(5-Br-qsal)₂Ni(dmit)₂·solv: Solvent effects, *Inorg. Chem.*, 2015, **54**, 1354–1362.

30   S. Hayami, K. Hiki, T. Kawahara, Y. Maeda, D. Urakami, K. Inoue, M. Ohama, S. Kawata and O. Sato, Photo-induced spin transition of iron(III) compounds with π-π intermolecular interactions, *Chem. - A Eur. J.*, 2009, **15**, 3497–3508.

31   T. Togo, S. A. Amolegbe, R. Yamaguchi, T. Kuroda-Sowa, M. Nakaya, K. Shimayama, M. Nakamura and S. Hayami, Crystal Structure and Spin-crossover Behavior of Iron(III) Complex with Nitroprusside, *Chem. Lett.*, 2013, **42**, 1542–1544.

32   J. Sirirak, W. Phonsri, D. J. Harding, P. Harding, P. Phommon, W. Chaoprasa, R. M. Hendry, T. M. Roseveare and H. Adams, Halogen substituted quinolylsalicylaldimines: Four halogens three structural types, *J. Mol. Struct.*, 2013, **1036**, 439–446.

33   Rigaku XRD; Rigaku Corporation. Tokyo, Japan, 2018.

34   CrysAlis Pro; Rigaku Corporation. Oxford, UK, 2019.

35   G. M. Sheldrick, Crystal structure refinement with SHELXL, *Acta Crystallogr. Sect. C Struct. Chem.*, 2015, **71**, 3–8.

36   G. M. Sheldrick, SHELXT – Integrated space-group and crystal-structure determination, *Acta Crystallogr. Sect. A Found. Adv.*, 2015, **71**, 3–8.

37   O. V. Dolomanov, L. J. Bourhis, R. J. Gildea, J. A. K. Howard and H. Puschmann, OLEX² : a complete structure solution, refinement and analysis program, *J. Appl. Crystallogr.*, 2009, **42**, 339–341.

38   V. Blum, R. Gehrke, F. Hanke, P. Havu, V. Havu, X. Ren, K. Reuter and M. Scheffler, Ab initio molecular simulations with numeric atom-centered orbitals, *Comput. Phys. Commun.*, 2009, **180**, 2175–2196.

39   J. P. Perdew, K. Burke and M. Ernzerhof, Generalized Gradient Approximation Made Simple, *Phys. Rev. Lett.*, 1996, **77**, 3865–3868.

40   A. Tkatchenko and M. Scheffler, Accurate Molecular Van Der Waals Interactions from Ground-State Electron Density and Free-Atom Reference Data, *Phys. Rev. Lett.*, 2009, **102**, 073005.

41   J. W. Furness, A. D. Kaplan, J. Ning, J. P. Perdew and J. Sun, Accurate and Numerically Efficient r²SCAN Meta-Generalized Gradient Approximation, *J. Phys. Chem. Lett.*, 2020, **11**, 8208–8215.

42   J. Cirera and E. Ruiz, Assessment of the SCAN Functional for Spin-State Energies in Spin-Crossover Systems, *J. Phys. Chem. A*, 2020, **124**, 5053–5058.

43   K. Nakamoto, *Infrared and Raman Spectra of Inorganic and Coordination Compounds*, John Wiley & Sons, Inc., Hoboken, NJ, USA, 2008.

44   B. J. C. Vieira, J. T. Coutinho, J. C. Dias, J. C. Nunes, I. C. Santos, L. C. J. Pereira, V. da Gama and J. C. Waerenborgh, Crystal structure and spin crossover behavior of the [Fe(5-Cl-qsal)₂][Ni(dmit)₂]·2CH₃CN complex, *Polyhedron*, 2015, **85**, 643–651.

45   R. Ketkaew, Y. Tantirungrotechai, P. Harding, G. Chastanet, P. Guionneau, M. Marchivie and D. J. Harding, OctaDist: a tool for calculating distortion parameters in spin crossover and coordination complexes, *Dalton Trans.*, 2021, **50**, 1086–1096.

46   W. Phonsri, D. J. Harding, P. Harding, K. S. Murray, B. Moubaraki, I. A. Gass, J. D. Cashion, G. N. L. Jameson and H. Adams, Stepped spin crossover in Fe(III) halogen substituted quinolylsalicylaldimine complexes, *Dalton Trans.*, 2014, **43**, 17509–17518.

47   D. J. Harding, W. Phonsri, P. Harding, K. S. Murray, B. Moubaraki and G. N. L. Jameson, Abrupt two-step and symmetry breaking spin crossover in an iron(III) complex: An exceptionally wide [LS-HS] plateau, *Dalton Trans.*, 2015, **44**, 15079–15082.

48   R. Díaz-Torres, J. Echeverría, O. Loveday, P. Harding and D. J. Harding, Interplay of halogen and hydrogen bonding in a series of heteroleptic iron(III) complexes, *CrystEngComm*, 2021, **23**, 4069–4076.

49   I. C. Berdiell, R. Kulmaczewski, N. Shahid, O. Cespedes and M. A. Halcrow, The number and shape of lattice solvent molecules controls spin-crossover in an isomorphous series of crystalline solvate salts, *Chem. Commun.*, 2021, **57**, 6566–6569.

50   L. J. K. Cook, R. Kulmaczewski, O. Cespedes and M. A. Halcrow, Different Spin-State Behaviors in Isostructural Solvates of a Molecular Iron(II) Complex, *Chem. - A Eur. J.*, 2016, **22**, 1789–1799.

51   C. F. Mackenzie, P. R. Spackman, D. Jayatilaka and M. A. Spackman, CrystalExplorer model energies and energy frameworks: extension to metal coordination compounds, organic salts, solvates and open-shell systems, *IUCrJ*, 2017, **4**, 575–587.

52   S. Hayami, Z. Z. Gu, H. Yoshiki, A. Fujishima and O. Sato, Iron(III) spin-crossover compounds with a wide apparent thermal hysteresis around room temperature, *J. Am. Chem. Soc.*, 2001, **123**, 11644–11650.

53   V. A. Money, J. Elhaïk, M. A. Halcrow and J. A. K. Howard, The thermal and light induced spin transition in [FeL$_2$](BF$_4$)$_2$(L = 2,6-dipyrazol-1-yl-4-hydroxymethylpyridine), *J. Chem. Soc. Dalton Trans.*, 2004, **4**, 1516–1518.

54   C. Bartual-Murgui, R. Diego, S. Vela, S. J. Teat, O. Roubeau and G. Aromí, A Spin-Crossover Molecular Material Describing Four Distinct Thermal Pathways, *Inorg. Chem.*, 2018, **57**, 11019–11026.

55   B. Weber, J. Obel, D. Henner-Vásquez and W. Bauer, Two new iron(II) spin-crossover complexes with N$_4$O$_2$ coordination sphere and spin transition around room temperature, *Eur. J. Inorg. Chem.*, 2009, 5527–5534.

56   E. Tailleur, M. Marchivie, N. Daro, G. Chastanet and P. Guionneau, Thermal spin-crossover with a large hysteresis spanning room temperature in a mononuclear complex, *Chem. Commun.*, 2017, **53**, 4763–4766.

57   J. Cirera, M. Via-Nadal and E. Ruiz, Benchmarking Density Functional Methods for Calculation of State Energies of First Row Spin-Crossover Molecules, *Inorg. Chem.*, 2018, **57**, 14097–14105.

58   S. Alvarez, P. Alemany, D. Casanova, J. Cirera, M. Llunell and D. Avnir, Shape maps and polyhedral interconversion paths in transition metal chemistry, *Coord. Chem. Rev.*, 2005, **249**, 1693–1708.

59   M. Llunell, D. Casanova, J. Cirera, P. Alemany and S. Alvarez, Shape program. 2010, Program for the Stereochemical Analysis of Molecular Fragments by Means of Continuous Shape Measures and Associated Tools, Universitat de Barcelona.

60   S. Alvarez, Relationships between Temperature, Magnetic Moment, and Continuous Symmetry Measures in Spin Crossover Complexes, *J. Am. Chem. Soc.*, 2003, **125**, 6795–6802.

61   S. Rackwitz, W. Klopper, V. Schünemann and J. A. Wolny, Quantification of intramolecular cooperativity in polynuclear spin crossover Fe(II) complexes by density functional theory calculations, *Phys. Chem. Chem. Phys.*, 2013, **15**, 15450.

ARTICLE   Journal Name

Table of Contents Entry

Structural and theoretical insights into solvent effects in an iron(III) SCO complex
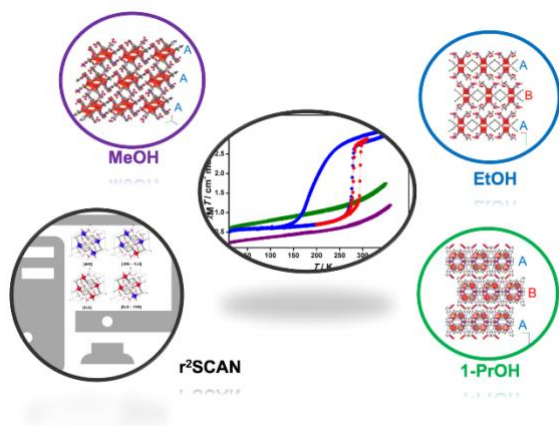
The impact of different alcohols on spin crossover properties is explored in a series iron(III) complexes